

ELASTIC SCATTERING OF 104 MeV ALPHA PARTICLES

G. HAUSER, R. LÖHKEN and H. REBEL

II. Physikalisches Institut der Universität Heidelberg, Germany

and

G. SCHATZ, G. W. SCHWEIMER and J. SPECHT

Kernforschungszentrum Karlsruhe, Zyklotron-Laboratorium, Germany

Received 23 December 1968

Abstract: Differential cross sections were measured for elastic scattering of 104 MeV alpha particles on ${}^6\text{Li}$, ${}^9\text{Be}$, ${}^{12}\text{C}$, ${}^{14}\text{N}$, ${}^{16}\text{O}$, ${}^{20}\text{Ne}$, ${}^{40}\text{Ar}$, ${}^{64}\text{Ni}$, ${}^{90}\text{Zr}$, ${}^{124}\text{Sn}$, ${}^{208}\text{Pb}$ and ${}^{209}\text{Bi}$. All angular distributions show a pronounced diffraction pattern. For the lightest nuclei measured (${}^6\text{Li}$ to ${}^{16}\text{O}$) the cross section exceeds the Rutherford cross section by a factor of up to 15 at angles around 45° . The cross section data were analysed in terms of parametrized phase-shift functions using 9 free parameters and in terms of the spinless optical model using up to 7 free parameters. Good fits were obtained. A strong absorption was found for the heavy nuclei, $A \geq 124$. For these nuclei, only the outermost region of the nuclear surface contributes to the scattering. A potential radius cannot be extracted regardless of the pronounced diffraction pattern. The absorption is not so strong for the medium weight nuclei, $A = 20$ – 90 . Information about the nuclear surface can be extracted from the differential cross section. The well known phase ambiguity in the optical model was found for these nuclei. For the light nuclei ($A \leq 16$) the inner region of the interaction potential contributes to the scattering. A repulsive core for small interaction distances explains the observed cross sections which indicates the nonlocal character of the true interaction.

The phase shift analysis leads to good fits, but the phase shifts obtained differ significantly from those of the optical-model analysis. This indicates that the phase-shift analysis is ambiguous also.

E

NUCLEAR REACTIONS ${}^6\text{Li}$, ${}^9\text{Be}$, ${}^{12}\text{C}$, ${}^{14}\text{N}$, ${}^{16}\text{O}$, ${}^{20}\text{Ne}$, ${}^{40}\text{Ar}$, ${}^{64}\text{Ni}$, ${}^{90}\text{Zr}$, ${}^{124}\text{Sn}$, ${}^{208}\text{Pb}$, ${}^{209}\text{Bi}(\alpha, \alpha)$, $E = 104$ MeV, measured $\sigma(\theta)$; deduced phase shifts and optical potentials. Enriched targets.

1. Introduction

The alpha-particle scattering in the medium energy range has frequently been investigated both experimentally and theoretically. Most of the investigations have been performed (${}^{1-11}$) at 42–44 MeV, and some experiments (${}^{12-14}$) were done at 65 MeV, while investigations at higher energies are scarce (${}^{15-17}$). Almost all of these studies have been motivated by the success in describing both elastic and inelastic cross sections by DWBA calculations or the Austern-Blair theory.

The optical model, usually applied in analogy with the scattering of nucleons, describes the elastic scattering of alpha particles fairly well (18,19). Good agreement between experimental and calculated cross sections has been obtained by choosing

suitable values of several parameters characterizing a complex potential. Nevertheless, there remains the difficulty that alpha particles are compound particles for which the validity of the optical model has not been established.

The obvious success of the optical model, e.g., in describing the diffraction pattern of the angular distributions, is based on the strong absorption. The de Broglie wavelength and the absorption length in nuclear matter are small compared to the nuclear dimensions so that the target nucleus appears black (with a diffuse edge) for the incoming particle. As a consequence the information about the interior of the nucleus is sparse, reflected by the known ambiguities^{20,21}). The concept of strong absorption is independent of the optical model. It can be exploited by a direct parametrization of the scattering function. Such a model was proposed by Akhiezer and Pomeranchuk²²) and Blair²³) (APB-Model) and generalized in a special way by Frahn and Venter²⁴). More recently Inopin²⁵) and Ericson²⁶) have formulated the black nucleus model in the Regge representation of the scattering amplitude. The direct way of parametrization of the scattering amplitude avoids the extensive computer calculations needed in the frame of the optical model and further leads to approximate analytical expressions of the cross sections in some special cases.

In this paper we report on experimental studies of the elastic scattering of 104 MeV alpha particles using the Karlsruhe isochronous cyclotron. The experiments were undertaken in view of the question: do the optical model (the applicability of which is a necessary prerequisite for DWBA analyses) and the concept of strong absorption describe the experimental cross sections at this energy satisfactorily? For heavy nuclei we found a sharp diffraction pattern due to strong absorption as seen for lighter nuclei at lower energies. Light nuclei, however, appear to be more transparent at our energy, and the basic concept of an opaque nucleus seems to become inapplicable. Due to the higher transparency, the alpha particles probe deeper into the nucleus and the ambiguities of the model parameters are thus removed.

2. Experimental procedure

2.1. BEAM OPTICS

Fig. 1 shows the layout of the beam line. The vertical and horizontal directions of the beam are adjusted by two steering magnets. A quadrupole triplet focusses the beam on a slit in front of the switching magnet. This slit is the only beam defining element in the system. A second quadrupole triplet behind the switching magnet focusses the beam on the target in the centre of the scattering chamber. The beam pipe behind the switching magnet holds two antiscattering diaphragms for reducing the background. The excitations of the various magnets and the width of the beam along the beam line were calculated[†] by means of an analogue computer^{††}, and

[†] We are indebted to Dipl.-Phys. D. Hartwig and Miss Chr. Rämmer for carrying out these calculations.

^{††} Particle track computer AERE No. 3037, purchased from C & N (Electrical) Ltd., England.

fine adjustments were done by viewing the beam spot on ZnS screens at the positions indicated in fig. 1 and at the centre of the scattering chamber. The diameter of the beam spot on the target was typically 2 mm. The horizontal phase space of the external deuteron beam of the Karlsruhe isochronous cyclotron has been measured to be $5.6 \text{ mm} \cdot \text{mrad}$ ²⁷⁾. Assuming this value also to be valid for the α -particle beam we obtain a divergence of the beam at the target of 0.16° (FWHM).

The extraction efficiency from the cyclotron was between 50 and 80 %, and the transmission of the slit amounted to approximately 30 %.

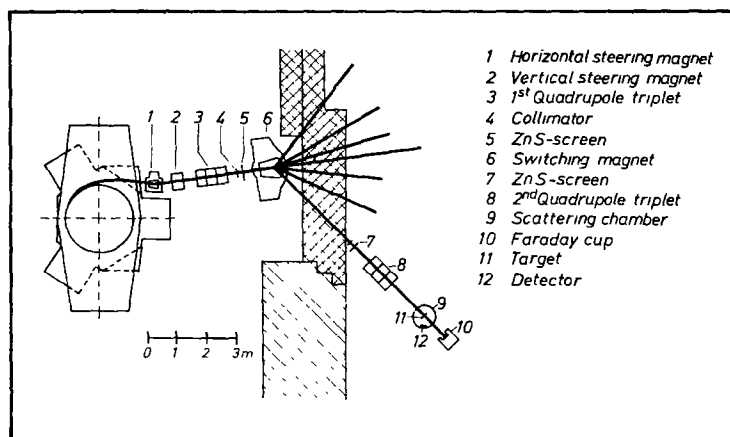


Fig. 1. The experimental layout.

2.2. SCATTERING CHAMBER

The scattering chamber [†] is cylindrical with an inner diameter of 70 cm and a height of 20 cm. The detector was mounted on a wheel inside the chamber close to the bottom. The wheel could be rotated by means of a precision drive which was adapted to this purpose from a machine tool. Drive and wheel were connected to the scattering chamber support such that deformation of the chamber during evacuation had no influence on the detector position. The angular position of the wheel could be read via a television camera to a precision of 0.02° . Foil targets were introduced from above through a vacuum lock.

2.3. TARGETS

The targets used were partly foils and partly gaseous. In all cases the isotopic abundance of the target isotope was about 99 %. Table 1 summarizes the relevant data.

The targets of ^6Li , ^9Be , ^{12}C , ^{64}Ni , ^{124}Sn , ^{208}Pb , and ^{209}Bi were foils without backing, the ^{90}Zr target was a deposit of ZrO_2 on melinex. All foil targets were

[†] The chamber was designed by Dr. B. Duelli and Dipl.-Phys. O. Meyer to whom we are indebted for placing it at our disposal.

circular, 14 mm in diameter. The thickness of the foil targets was measured by weighing and by measuring the energy loss of ^{241}Am α -particles.

The gas targets were cylindrical sealed off containers made of brass and sized 140 mm diam. \times 35 mm. A 10 mm high slit that ran almost all around the cylinder and that was covered by a 6 μm thick havar foil providing an entrance and exit for the primary beam and the scattered particles. These target containers were filled to approximately 1 atmosphere. The pressure was checked before and after measurement. The effective target thickness²⁸⁾ was defined by the 1.7 \times 6 mm entrance slit of the detector and a second 3 mm wide slit placed 225 mm in front of the detector.

TABLE 1
Target data

Target isotope	Thickness (mg/cm ²)	Isotopic abundance	Form	Remarks
^6Li	4.37	99.3	metal foil	d)
^9Be	13.56	100	metal foil	
^{12}C	18.05	98.9	foil	
^{14}N	0.52	99.6	gas	a)
^{16}O	0.45	99.8	gas	a)
^{20}Ne	0.38	99.9	gas	a, b)
^{40}Ar	0.76	99.6	gas	a)
^{64}Ni	4.88	99.2	metal foil	c)
^{90}Zr	4.22	97.5	ZrO ₂ on melinex	c)
^{124}Sn	5.56	99.3	metal foil	c)
^{208}Pb	8.02	99.2	metal foil	c)
^{209}Bi	6.15	100	metal foil	

a) Effective target thickness at 90° scattering angle.

b) Obtained from Mound Laboratory, Miamisburg.

c) Obtained from AERE, Harwell.

d) Obtained from ORNL.

An additional check of all target thickness determinations was provided by the scattering data themselves. When the data were analysed according to the models described in sect. 4 it became evident that the cross section below 8° scattering angle is virtually independent of the nuclear parameters for a wide range around the best set of parameters. This is due to the dominating influence of Rutherford scattering at small angles.

All independent thickness determinations of a specific target agreed to within 5 %[†].

2.4. DETECTORS AND ELECTRONICS

All data given in this paper were taken with Si(Li) detectors of area 100 mm². The detectors were mounted inside a copper block of 38 mm diameter with an en-

[†] An exception to this was a measurement on ^{140}Ce which was reported in a preceding publication¹⁷⁾. The target consisted of cerium oxide on a carbon backing. Due to the uncertain chemical composition the results of different thickness determinations differed by up to a factor of 4. These data have, therefore, not been included in the present analysis, and the absolute cross section is more inaccurate than indicated by the 25 % error quoted previously.

trance slit of $1.7 \times 6 \text{ mm}^2$ at a distance of 300 mm from the target center. The calculated angular resolution of this system is 0.6° assuming a beam diameter of 2 mm and an angular divergence of 0.2° . The detectors allowed measurements down to 4.0° in the laboratory system. The copper housing of the detectors was cooled with water at 0° C .

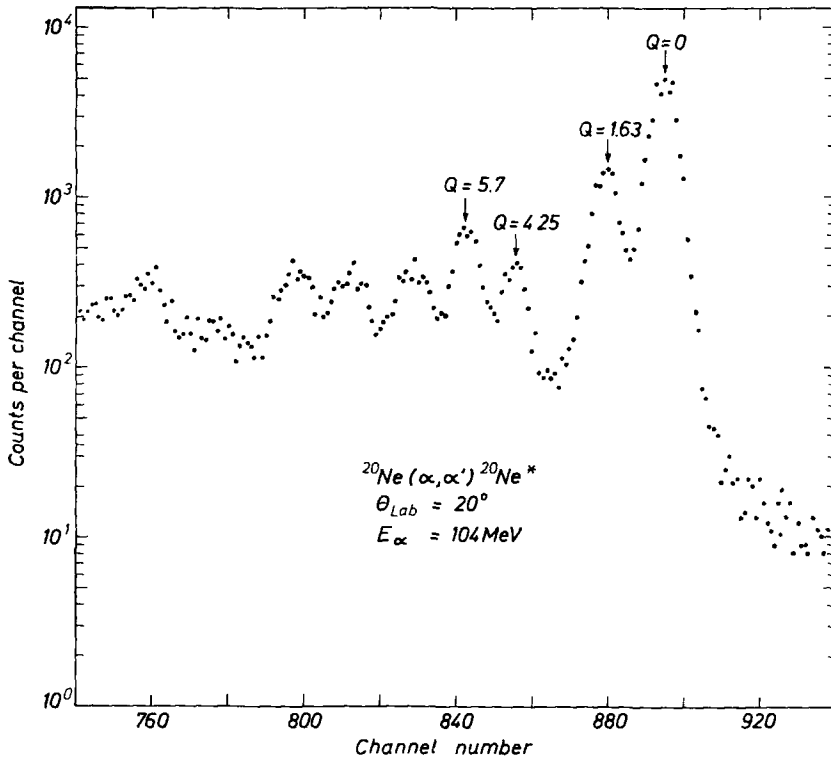


Fig. 2. Energy spectrum of alpha particles scattered elastically and inelastically by ^{20}Ne at 104 MeV incident energy and 20° scattering angle (lab. system) measured with a 5 mm Si(Li) detector.

Two detectors of 3 mm and 5 mm depletion depth, respectively, have been used in the course of the experiments. As the range of 104 MeV alpha particles in silicon is approximately 4 mm an aluminium absorber in front of the 3 mm thick detector was used in order to degrade the energy of the scattered particles. This resulted in an energy spread of 1.2 MeV. A resolution between 300 and 600 keV was obtained with the thick detector. Most of this line width is attributed to the energy spread of the primary beam. Fig. 2 shows a spectrum taken with the 5 mm thick detector.

No particle identification was applied during the measurements presented in this

paper. This is unnecessary as the maximum energy loss of protons, deuterons, ^3H and ^3He nuclei is 31, 42, 50 and 108 MeV, respectively, in 5 mm silicon. So only ^3He particles could possibly cause detector pulses in the energy region of interest in elastic alpha-particle scattering. Due to the large difference in binding energies between ^3He and ^4He the maximum energy of ^3He particles produced is considerably lower than that of the elastically scattered alpha particles.

The electronics consisted of a preamplifier, an amplifier, and a base-line restorer (Ortec models 105, 410 and 438, respectively). The pulses were then fed to an ADC which was directly coupled to a CDC 3100 on-line computer.

2.5. DATA ACQUISITION

For most of the angular range data were taken at 0.5° intervals. The smallest angle of measurement was between 4° and 5° (laboratory system), the largest was determined by the magnitude of the cross section. Most targets were measured down to a differential cross section of $10 \mu\text{b/sr}$. The zero of the angular scale was determined by measuring the cross section on either side of the incident beam for small scattering angles. It was possible to establish the zero to an accuracy of 0.1° due to the strong variation of cross section at small scattering angles.

The incident current was adjusted to keep the deadtime losses below 10 %. It varied between 0.05 nA and $1 \mu\text{A}$ depending on scattering angle and target thickness. It was integrated by means of an Elcor model A309B current integrator. The integrator initiated and stopped data storage via the computer interrupt system.

The CDC 3100 on-line computer was programmed as a 1024-channel pulse-height analyser. The program included a routine to sum the spectrum between two selectable channels and to correct the sum for a linear background and for deadtime. The spectra were recorded on magnetic tape for further processing.

For some targets the peaks of elastically and inelastically scattered alpha particles overlapped and had to be separated by means of a Fortran program on an IBM 7074 computer.

2.6. ESTIMATE OF ERRORS

The errors of the individual experimental results shown in figs. 3 to 5 include

- (i) the statistical error which is negligible for most points and
- (ii) an error due to the uncertainty of the angle of measurements (0.1°). This error is due to the uncertainty of the angular scale zero and was converted into an error of the cross section by multiplying it by the slope of the measured cross section.

The errors of the absolute value of the cross section due to inaccuracies of target thickness, solid angle, and current measurements are estimated to be 5 % and have not been included in the error bars shown in the figures.

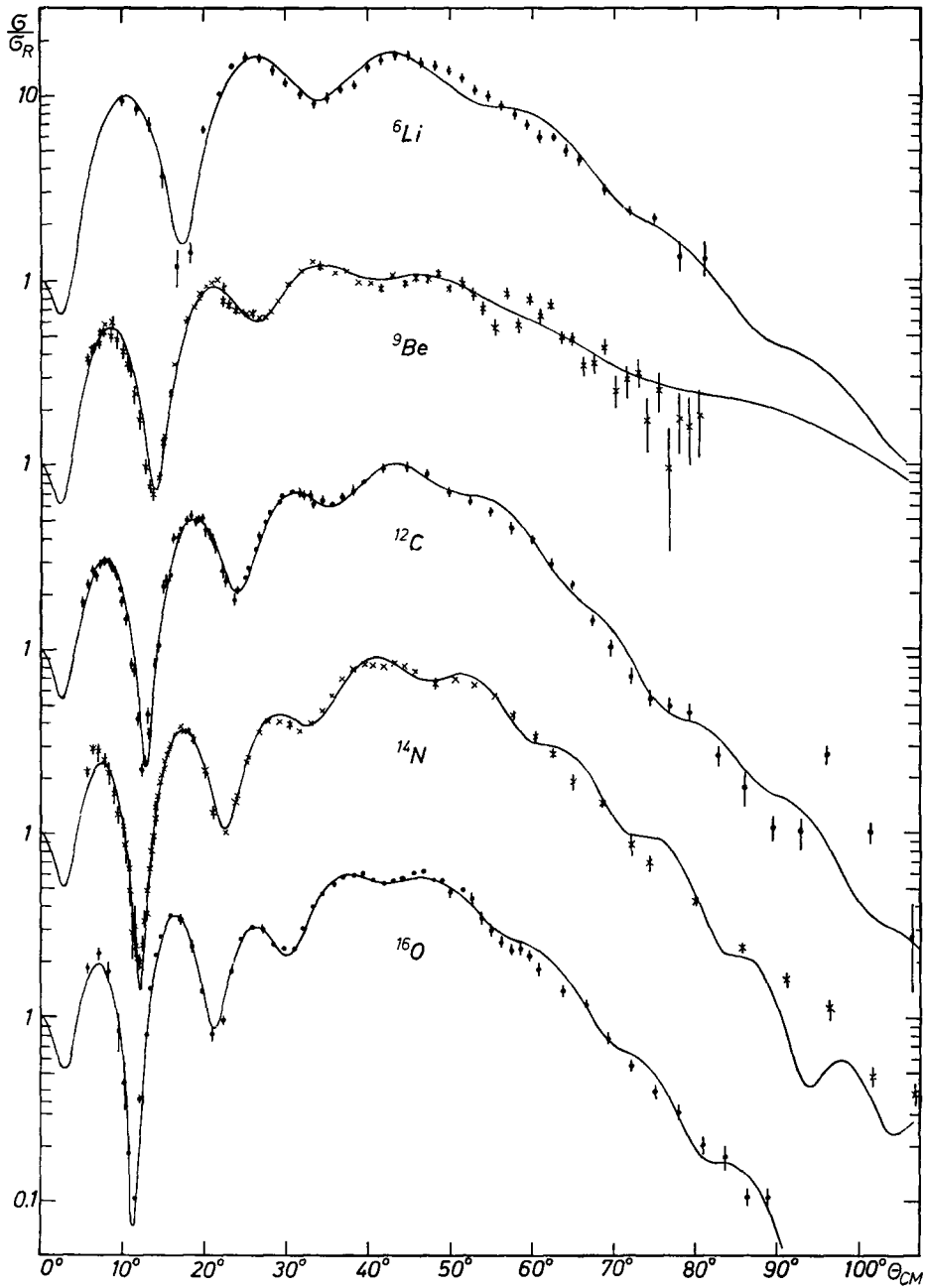


Fig. 3. Cross sections of the elastic scattering of 104 MeV alpha particles. Experimental errors are indicated where they exceed 4 %. The solid curves show the results of the phase-shift analysis.

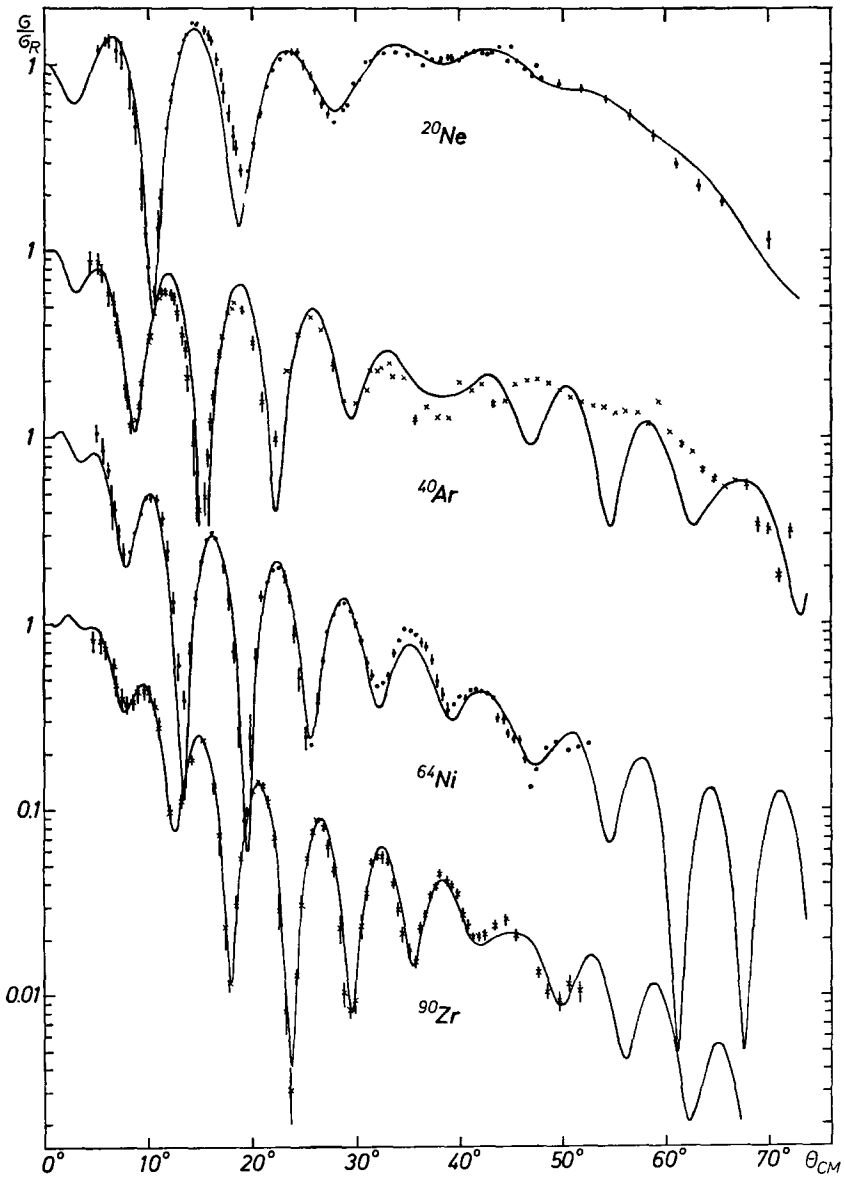


Fig. 4. Cross sections for the elastic scattering of 104 MeV alpha particles. Experimental errors are indicated where they exceed 4 %. The solid curves show the results of the phase-shift analysis.

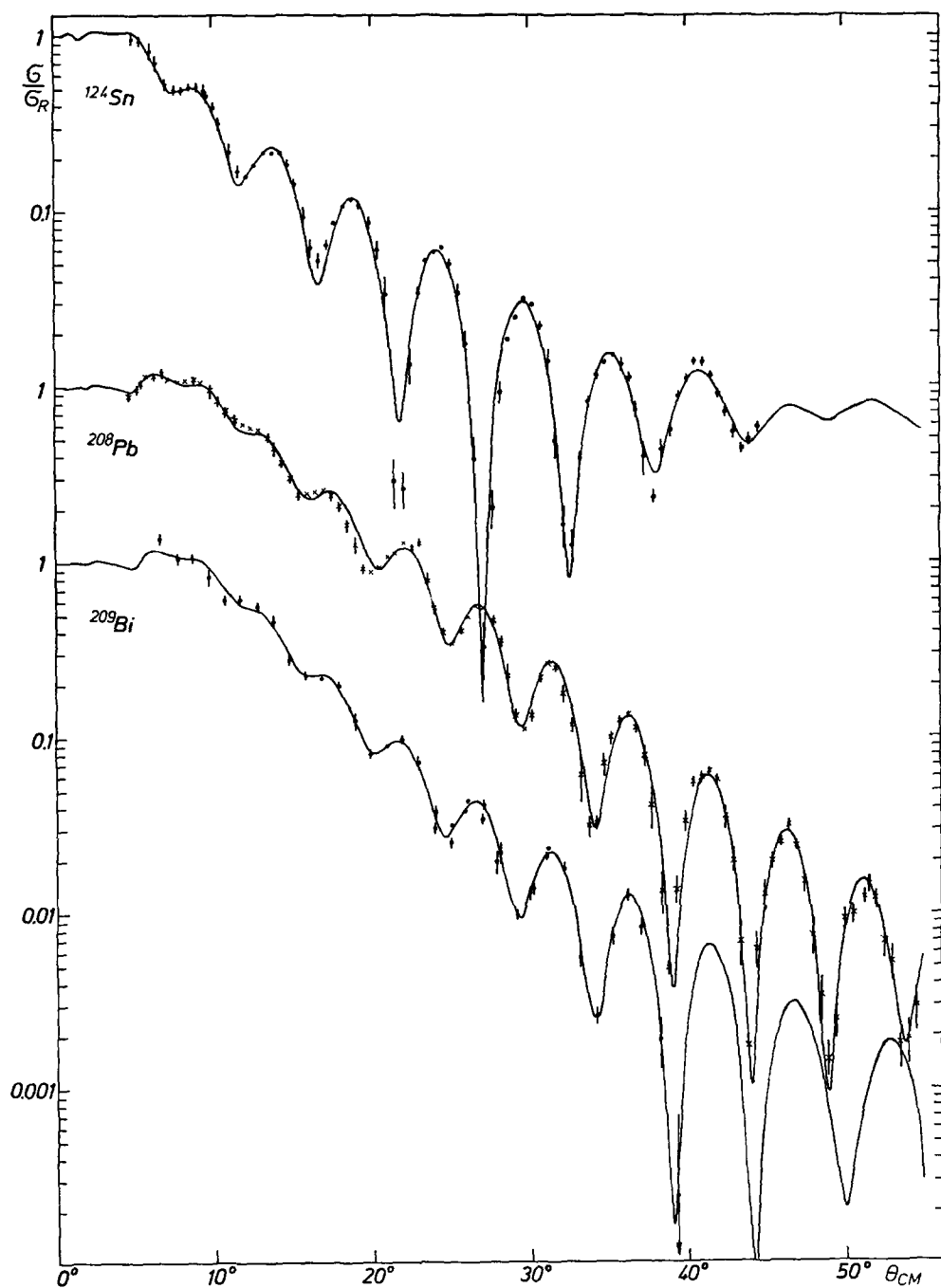


Fig. 5. Cross sections for the elastic scattering of 104 MeV alpha particles. Experimental errors are indicated where they exceed 4 %. The solid curves show the results of the phase-shift analysis.

3. Results

The measured cross sections[†] normalized to the Rutherford cross section are shown in figs. 3 to 5. The curves are theoretical results and will be discussed in the following section.

For the heavier nuclei the curves exhibit a pronounced and regular diffraction pattern which had not been observed at forward angles at lower energies. The results for the lighter elements are somewhat more unexpected. The oscillations which are very pronounced at small scattering angles are soon damped, and the cross sections show a broad maximum around 45°. In this region the cross sections exceed the Rutherford cross section considerably (by up to a factor of 15 for ⁶Li). The height of this maximum decreases steadily from ⁶Li to ¹⁶O, and it has virtually vanished for ²⁰Ne.

The amplitude of the oscillations of the cross section shows a maximum which is shifted from about 10° for ⁶Li to 45° for ²⁰⁸Pb. Beyond the maximum the oscillation is rapidly damped. A new increase of the oscillation as predicted by different models could not be found.

4. Data analysis

The elastic scattering cross section $\sigma(\theta)$ is given by the absolute square of the scattering amplitude $f(\theta)$, which can be expanded in the following way

$$f(\theta) = f_c(\theta) + (2ik)^{-1} \sum_{l=0}^{\infty} (2l+1)(S_l - 1) \exp(2i\sigma_l) P_l(\cos \theta). \quad (1)$$

Here, θ is the scattering angle, k is the wave number, $f_c(\theta)$ is the Coulomb scattering amplitude, σ_l are the Coulomb phase shifts, S_l are the partial scattering amplitudes relative to the Coulomb scattering and $P_l(\cos \theta)$ are the Legendre polynomials. In the following analysis the nonrelativistic expressions were used

$$k = (2mc^2 E)^{1/2} / \hbar c, \quad \hbar c = 197.315 \text{ MeV} \cdot \text{fm},$$

where mc^2 is the reduced mass and E the center-of-mass energy. The Coulomb phase shifts were calculated with the recurrence relation

$$\sigma_{l-1}(\eta) = \sigma_l(\eta) - \text{arctg}(\eta/l), \quad (2)$$

starting from $\sigma_3(\eta)$ which is directly obtained from the asymptotic series expansion for large l values³⁰). The Coulomb scattering amplitude is given by

$$f_c(\theta) = - \frac{\exp \{2i[\sigma_0 - \eta \ln(\sin \frac{1}{2}\theta)]\}}{2k \sin^2 \frac{1}{2}\theta}, \quad (3)$$

and the Coulomb parameter is $\eta = \alpha Z/\beta$ where Z is the product of the charge numbers, α the hyperfine structure constant and β the relative velocity in units of c .

[†] For numerical results see ref. ²⁹).

The partial scattering amplitudes S_l are related to the complex phase shifts δ_l by

$$S_l = \exp [2i(\delta_l - \sigma_l)]. \quad (4)$$

Spin orbit terms can contribute to the scattering in the cases of ${}^6\text{Li}$, ${}^9\text{Be}$ and ${}^{14}\text{N}$. This contribution is expected to be small and has therefore been neglected.

The partial scattering amplitudes S_l will be obtained in two different ways. a) Assuming that the S_l may be represented by a continuous function of the quantum number l , a direct parametrization of this function is introduced. b) Assuming that the interaction of the alpha particle with the target nucleus may be considered as a spinless two body problem with a complex interaction potential $V(r)$ the Schrödinger equation may be solved to obtain the amplitudes S_l . In this case the interaction potential $V(r)$ is parametrized. The radial Schrödinger equation

$$U_l''(\rho) + \left[1 - \frac{V(r)}{E} - \frac{l(l+1)}{\rho^2} \right] U_l(\rho) = 0, \quad \rho = kr, \quad (5)$$

is integrated numerically from $r = 0$ to an outside point $r = R_\psi$ where the potential $V(r)$ differs by less than 10 keV from the Coulomb potential. At this point the partial scattering amplitude is given by the logarithmic derivative U_l'/U_l and the Coulomb wave functions F_l and G_l

$$\frac{U_l'}{U_l} = \frac{F_l' + iG_l' + S_l(F_l' - iG_l')}{F_l + iG_l + S_l(F_l - iG_l)}, \quad r = R_\psi. \quad (6)$$

The fitting program consists of a general χ^2 minimizing subroutine ³¹⁾† with small subroutines for calculating the quantities S_l , $V(r)$ and the Coulomb functions, and the driving main program ³²⁾. The fitting procedure minimizes the sum

$$\chi^2 = \sum_{i=1}^N [\sigma_{\text{exp}}(\theta_i) - \sigma_{\text{th}}(\theta_i)]^2 / \Delta\sigma_{\text{exp}}^2(\theta_i). \quad (7)$$

The computations were carried out with the Karlsruhe IBM 7074 computer ^{††}.

4.1. PHASE-SHIFT ANALYSIS

In the elastic scattering of 104 MeV alpha particles the number of partial waves contributing to the sum in eq. (1) is sufficiently large (up to 60) to consider the coefficients S_l as continuous functions of the angular momentum number l . The function $S(l) = S_l$ obtained from optical-model calculations at lower energies suggested the parametrizations proposed by Akhiezer and Pomeranchuk ²²⁾ and by Frahn and

† We thank Dr. M. J. D. Powell for making available the Fortran code of the subroutine.

†† Some preliminary calculations were done with the Abacus code ³³⁾ with the IBM 7090 Computer of the Institut für Hochenergiephysik der Universität Heidelberg.

Venter ²⁴). The expressions for the S_l functions are

$$\begin{aligned} |S_l| &= \varepsilon_1 + (1 - \varepsilon_1) \{1 + \exp [(l_1 - l)/\delta_1]\}^{-1}, \\ \arg S_l &= \mu \{1 + \exp [(l - l_2)/\delta_2]\}^{-1}, \end{aligned} \quad (8)$$

in the APB model, and

$$\begin{aligned} \operatorname{Re} S_l &= \varepsilon_1 + (1 - \varepsilon_1) \{1 + \exp [(l_1 - l)/\delta_1]\}^{-1}, \\ \operatorname{Im} S_l &= \mu \exp [(l_2 - l)/\delta_2] \{1 + \exp [(l_2 - l)/\delta_2]\}^{-2} \\ &\quad + \varepsilon_2 \{1 + \exp [(l - l_1)/\delta_1]\}^{-1}, \end{aligned} \quad (9)$$

in the model of Frahn and Venter. The parametrization of Frahn and Venter restricts the value of $\arg S_l$ to values smaller than 360° .

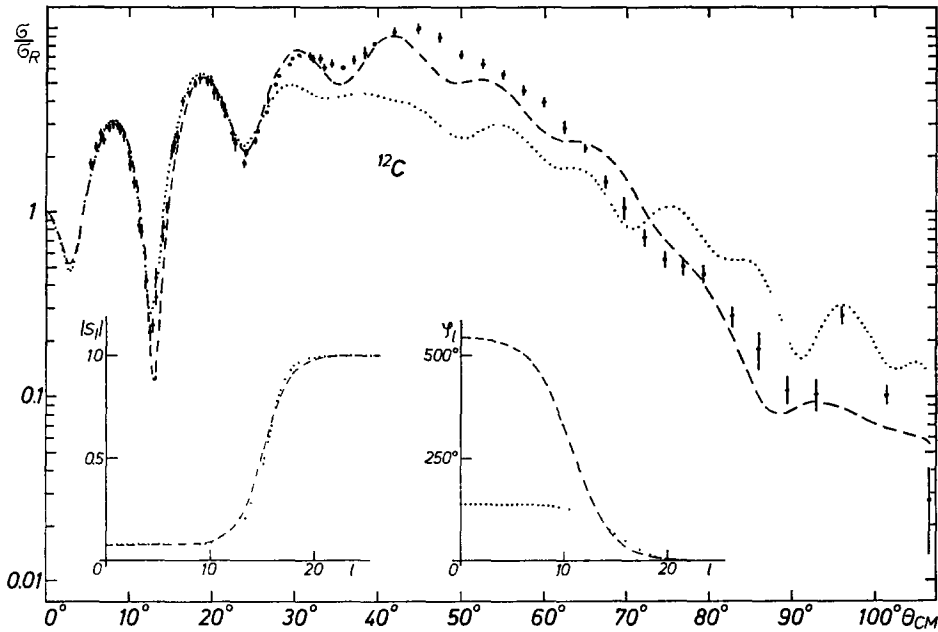


Fig. 6. Fits to the ^{12}C data obtained with the parametrization of the phase shifts by the APB model (dashed curves) and by Frahn and Venter (dotted curves).

TABLE 2

Parameters for the best fits of the ^{12}C data with the Frahn and Venter, and the APB parametrization of the S_l function

	ε_1	ε_2	l_1	l_2	δ_1	δ_2	μ	χ^2/F
Frahn and Venter	-0.0592	0.0550	16.026	16.167	0.871	1.223	0.1235	38.9
APB	0.0775		15.056	10.779	1.285	1.937	9.531	10.9

The meaning of the symbols is given in equations (8) and (9).

With these parametrizations good fits were obtained for the heavy nuclei only. Fig. 6 shows the bad quality of the fits for the ^{12}C data; in table 2 the corresponding parameters of the best fits are given. The values $|S_l|$ are similar in both fits but the $\arg S_l$ differ considerably for the small partial waves.

The reason why the cross sections of light nuclei cannot be reproduced with the parametrizations (8) and (9) is the finite transmission of the partial waves with angular momentum numbers less than 10. Hence we introduced a more general parametrization ¹⁷⁾

$$|S_l| = \varepsilon + (1 - \varepsilon) \{1 + \exp [(L - l)/\delta_1]\}^{-1}, \quad (10)$$

$$\arg S_l = [a_0 + a_1(l - L) + \dots + a_4(l - L)^4] \{1 + \exp [(l - L)/\delta_2]\}^{-1}.$$

The values of $|S_l|$ are the same as in the APB model but the $\arg S_l$ are now given by a polynomial multiplied by a step function.

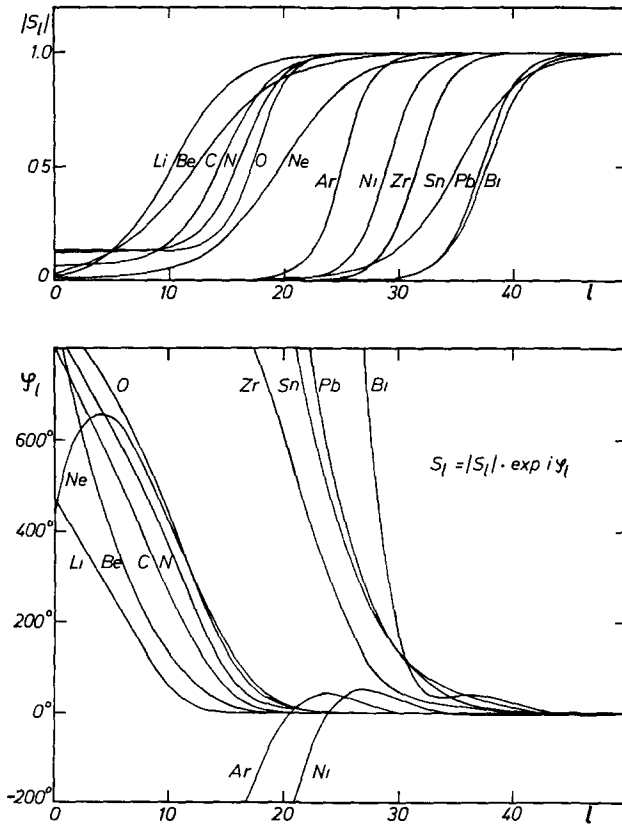


Fig. 7. Phase-shift functions obtained from the best fits shown in figs. 3 to 5.

TABLE 3
Parameters for the best fits with the generalized parametrization of the phase-shift functions

Target	L	ϵ	$4\delta_1$	$4\delta_2$	a_0	$a_1 10^2$	$a_2 10^2$	$a_3 10^3$	$a_4 10^4$	χ^2/F	χ^2_c/F	L_1	$\sigma_R(b)$
^6Li	10.235	$2 \cdot 10^{-7}$	10.774	4.956	1.816	-24.91	7.712	4.491	0.5173	5.53	1.87	25	0.864
^9Be	12.194	$5 \cdot 10^{-7}$	14.851	6.510	2.256	-15.17	4.239	-4.885	-1.582	2.85	2.95	30	0.990
^{12}C	14.582	0.067	8.738	5.241	2.089	-17.44	12.01	7.463	1.581	2.59	1.07	35	0.840
^{14}N	16.380	0.128	7.221	4.748	1.649	-3.008	19.15	15.53	4.145	4.69	2.68	24	0.880
^{16}O	17.575	0.131	5.799	4.171	1.753	16.19	21.91	15.20	3.307	3.72	1.47	40	0.906
^{20}Ne	19.687	0.010	12.677	9.994	0.778	-29.42	2.792	-3.946	-2.646	4.79			1.286
^{40}Ar	25.050	0.009	5.401	3.660	1.251	42.73	14.19	30.00	12.85	54.47			1.387
^{64}Ni	28.974	0.003	6.065	13.241	1.363	-8.305	-3.501	4.633	-2.860	12.33			1.719
^{90}Zr	31.601	0.003	5.979	8.872	1.105	3.907	5.983	-4.451	-2.778	2.99			1.950
^{132}Sn	35.134	0.008	11.194	7.765	1.068	-6.557	2.762	-2.490	-0.0994	4.20			2.508
^{208}Pb	37.202	0.005	6.427	9.362	1.109	-5.471	-0.7944	-3.072	0.7789	3.39			2.540
^{209}Bi	37.658	0.005	7.236	5.451	1.291	25.26	4.311	13.55	21.02	1.90			2.628

F = number of measurement points minus 9.

χ^2_c/F = fit corrected for $l = 0$ up to $l = L_1$, see subsect. 4.3.

σ_R = reaction cross section computed with the S_l values of the best fit. The meaning of the remaining symbols is explained in subsect. 4.1, expression (10).

With this parametrization the fits were considerably improved. The results are shown in figs. 3 to 5. Table 3 summarizes the best fit parameters and fig. 7 shows the resulting S_l functions. The fit to the ^{20}Ne data shows systematic deviations around 17° , and the fit to the ^{64}Ni data around 35° . The fit to the ^{40}Ar data is poor for scattering angles beyond 45° . Such statistically significant deviations of the best fit curves from the experimental data manifest an inherent limitation of the used parametrizations.

4.2. OPTICAL-MODEL ANALYSIS

In the optical-model calculations the Coulomb potential V_C was deduced from experimental nuclear charge distributions ³⁴). The numerically computed Coulomb potential was fitted by a polynomial of order 6 for values of r where the charge density is not zero. The coefficients of the polynomials were not varied in the subsequent optical-model analysis of the experimental cross section data.

The nuclear potential V_N was used in two different parametrizations:

(a) The Woods-Saxon form

$$V_N(r) = (V_0 + iW_0)\{1 + \exp[(r - R)/a]\}^{-1}, \quad V_0 \text{ and } W_0 < 0, \quad (11)$$

in the usual meaning of the symbols for the four parameters V_0 , W_0 , R and a .

(b) A nuclear potential composed of bell-shaped functions generating a form factor similar to that of a "wine bottle" potential

$$\begin{aligned} V_N(r) &= V_0 g_v(r) + iW_0 g_w(r), \\ g(r) &= 4 \exp(x) / [1 + \exp(x)]^2, \\ x &= \begin{cases} 3.525(r - R_i)/a_i^-, & r \leq R_i \\ 3.525(r - R_i)/a_i^+, & r > R_i, \end{cases} \quad i = v, w. \end{aligned} \quad (12)$$

The coefficients in the form factors $g(r)$ are chosen in such a way that they have their maxima normalized to 1 at $r = R_i$ and their FWHM is $\frac{1}{2}(a_i^+ + a_i^-)$. We introduced two values of a in order to allow asymmetrical form factors.

A form factor similar to that in expression (11) (Woods-Saxon) is obtained by setting

$$a_i^- = \infty, \quad a_i^+ = 5.2a, \quad R_i = R - 2.6a \quad \text{for } i = v, w.$$

The potential form (12) was introduced as the four parameter Woods-Saxon potential is not able to reproduce the elastic scattering for the light nuclei. In fig. 8 we show the best fit for the ^{12}C data using the Woods-Saxon form factor. At the minimum of χ^2 the real potential depth found is 70 MeV starting from 35 and 150 MeV in the fitting procedure. Further test calculations with potential depths up to 200 MeV let us conclude that the χ^2 minimum found at $-V_0 = 70$ MeV is the only one for $-V_0 \leq 200$ MeV.

Using the expression (12) with six free parameters: V_0 , W_0 , R_v , R_w , a_v^+ and a_w^+ ($a_v^- = a_w^- = \infty$) better agreement is obtained (see fig. 8). Nevertheless the fit is poor compared to that deduced from the phase-shift analysis. A considerable improvement is achieved with asymmetrical bell-shaped form factors for both the real and the imaginary parts, defined by up to eight free parameters altogether in expression (12).

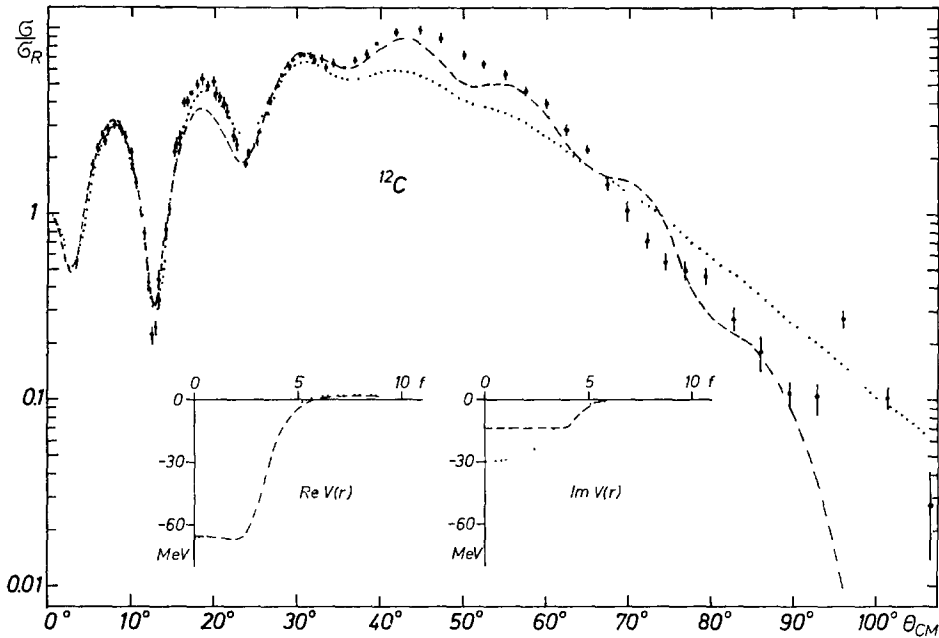


Fig. 8. Best fits to the ^{12}C data obtained with 4 (dotted curves) and 6 (dashed curves) parameters in the optical potentials shown. The potentials include the Coulomb potential.

Fig. 9 presents the best fits for the 7 parameter interaction potential of ^6Li , ^9Be , ^{12}C , ^{14}N , and ^{16}O . Fig. 12 shows the corresponding potentials † . A well-type imaginary form factor proves to be the best. Therefore the parameter a_w^- was not varied in the final analysis. The influence of the central region of the interaction potential is demonstrated in fig. 13.

The experimental results for the medium weight nuclei are described well enough using only six free parameters. This is due to the reduced contribution of the interior of the nucleus. As an example we show in fig. 14 the almost identical scattering cross sections for ^{64}Ni resulting from two potentials differing in the central region of the real part of V_N . There is a continuous ambiguity for the value of the potential

† The cross section of ^9Be is best described with the potential shown in fig. 12; but test calculations with wine bottle potentials reproduce the cross section almost equally well.

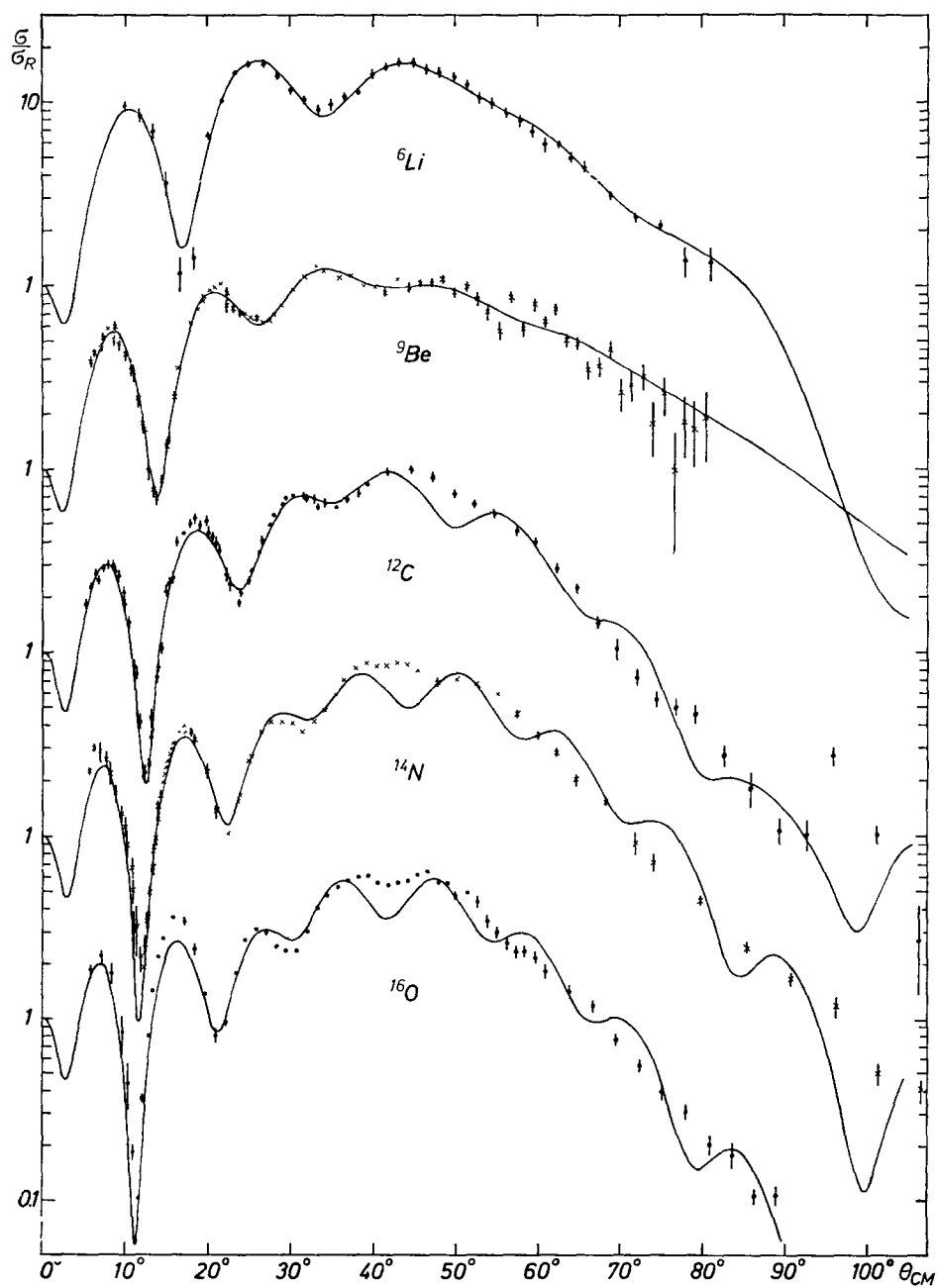


Fig. 9. Best optical-model fits to the elastic scattering cross sections obtained with 7 free parameters.

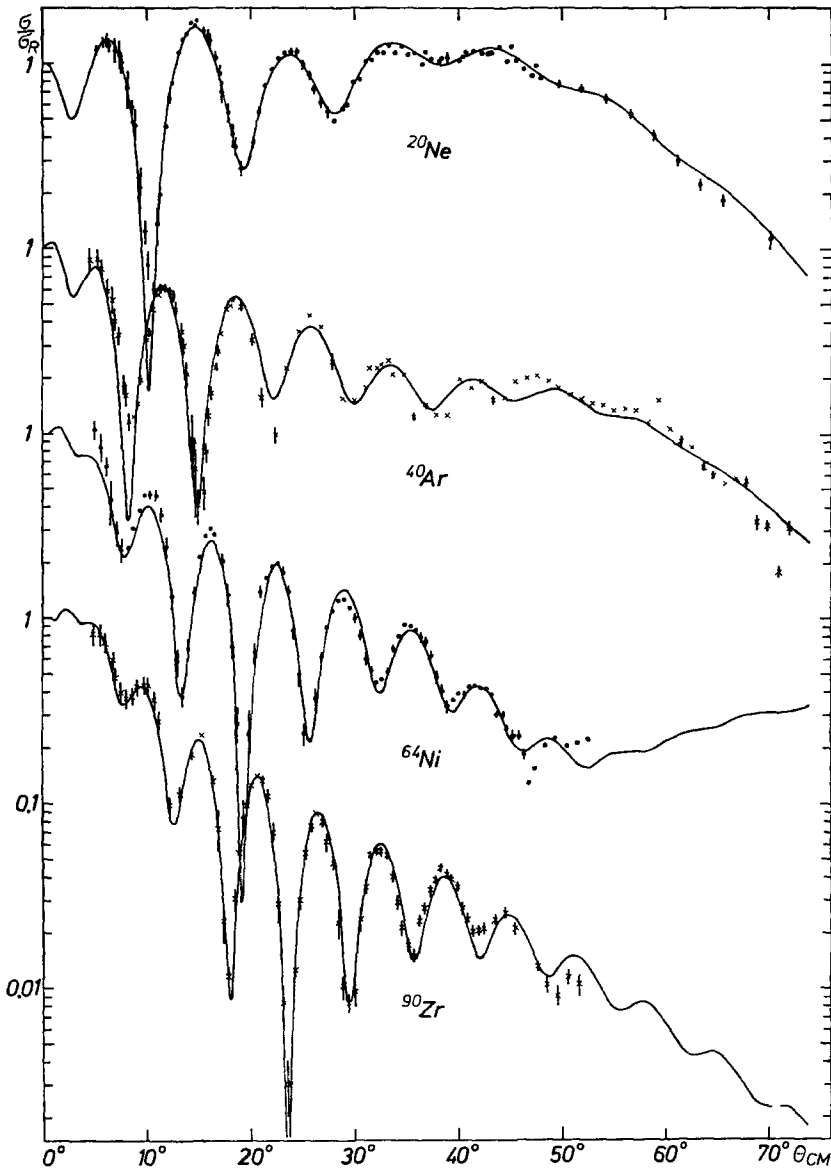


Fig. 10. Best optical-model fits to the elastic scattering cross sections obtained with 6 free parameters.

parameter a_v^- . The potential part for $r > R_i$ is ambiguous, too. Here the known phase ambiguity^{20,21)} was found. There exist at least two discrete sets of parameters which describe the ^{64}Ni cross sections equally well (see table 4).

The situation for the heavy nuclei ^{124}Sn , ^{208}Pb , and ^{209}Bi becomes extreme.

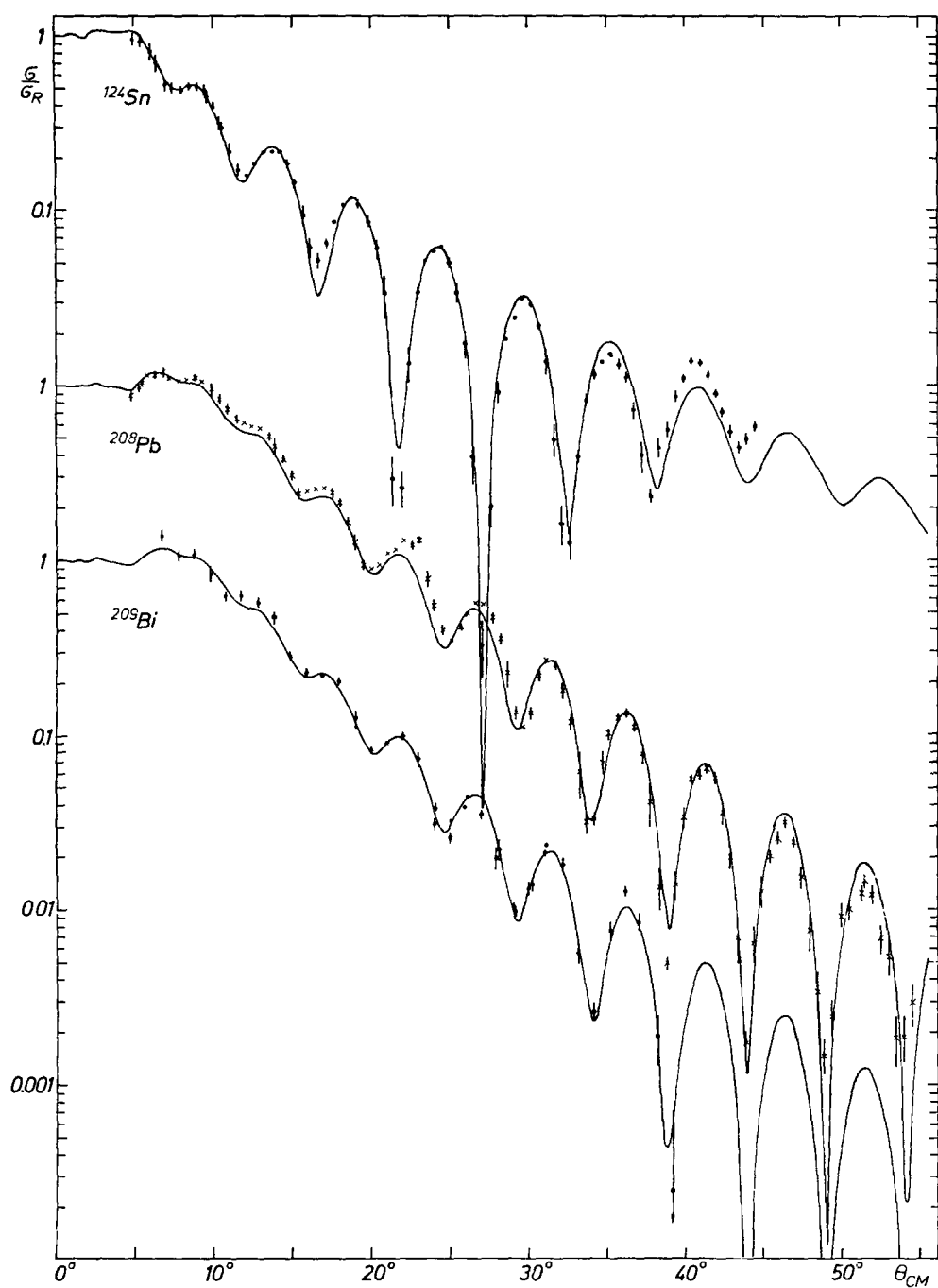


Fig. 11. Best optical-model fits to the elastic scattering cross sections obtained with 3 free parameters.

Only the outermost region of the nuclear surface contributes to the scattering. In this region expression (11) reduces to ^{19,12,7)}

$$V_N(r) = (V_0 + iW_0) \exp(R/a) \exp(-r/a), \quad (r-R)/a > 1. \quad (13)$$

Expression (13) clearly shows that the radius R of the interaction potential cannot be determined, regardless of the pronounced diffraction pattern of the scattering cross section. Therefore we chose arbitrarily a depth of 60 MeV for the real part of

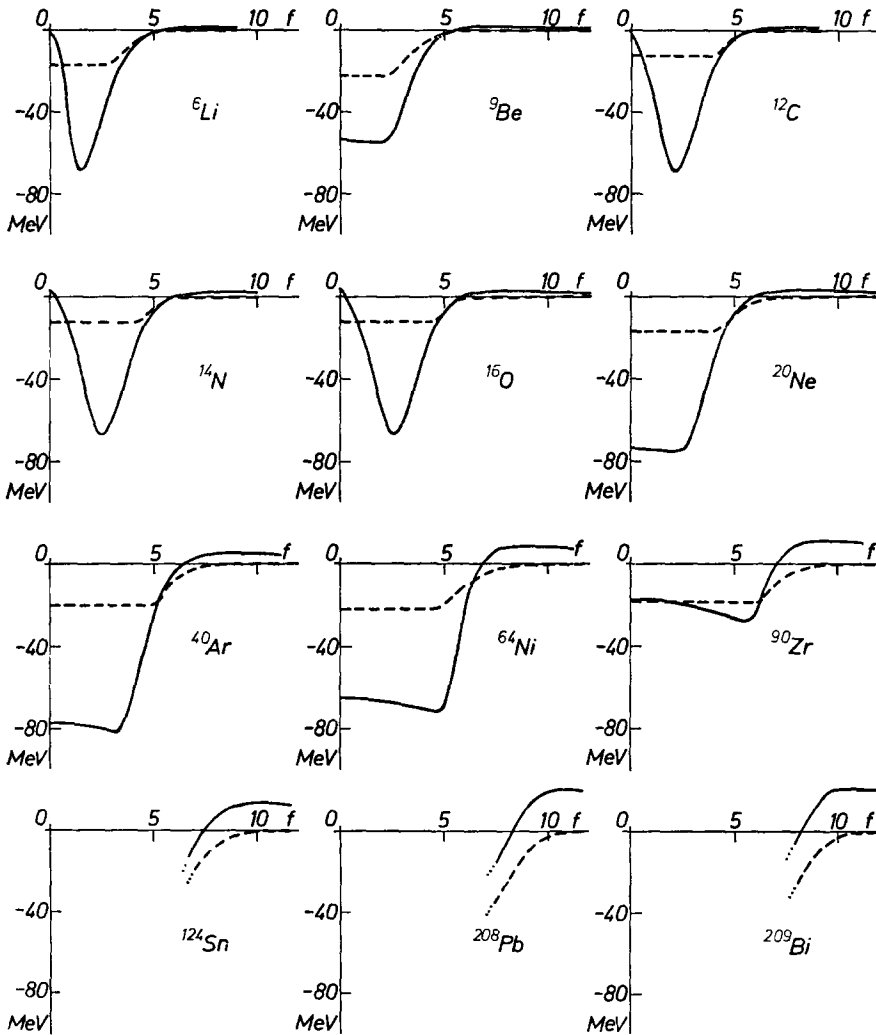


Fig. 12. Optical potentials obtained from the analysis of the elastic scattering cross sections. The sum of the Coulomb and nuclear potentials is shown. Solid curves show the real part and dashed curves the imaginary part of the optical potential. The inner part of the potential is not shown for the heavy nuclei because this part does not contribute to the scattering.

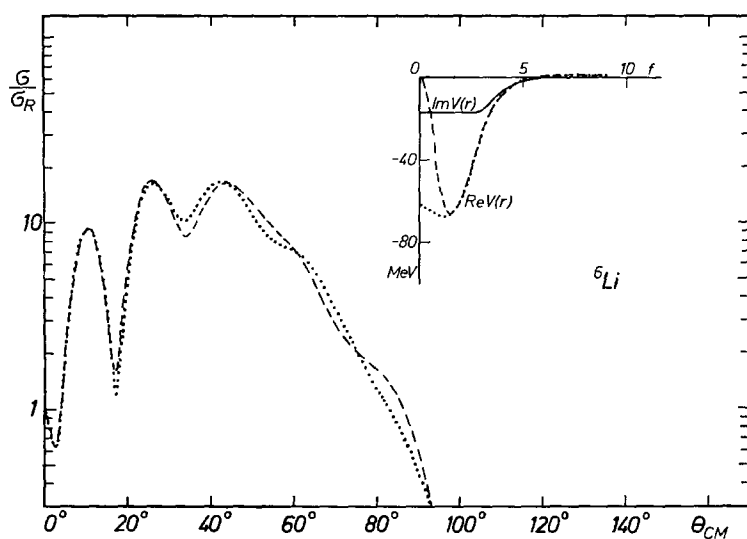


Fig. 13. Influence of the real part of the optical potential for small interaction distances on the elastic scattering of 104 MeV alpha particles by ${}^6\text{Li}$.

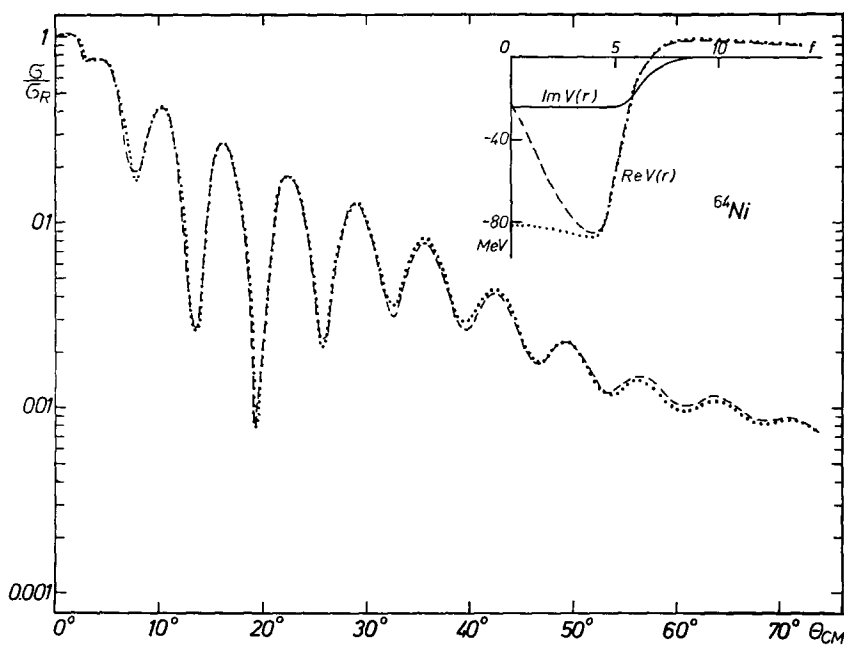


Fig. 14. Influence of the real part of the optical potential for small interaction distances on the elastic scattering of 104 MeV alpha particles by ${}^{64}\text{Ni}$.

the nuclear potential. As a check for ^{209}Bi a very large potential was used setting arbitrarily $R = 4$ fm, $V_0 = -19$ GeV and $W_0 = -13.8$ GeV in expression (13). The two calculated cross sections are shown in fig. 15. The experimental points lie between the two curves. Figs. 10 and 11 show the best fits for the medium weight and heavy nuclei, fig. 12 the corresponding potentials. The results of the optical-model calculations are summarized in table 4. For comparison with the phase-shift calculations the corresponding S_l values are given in fig. 16.

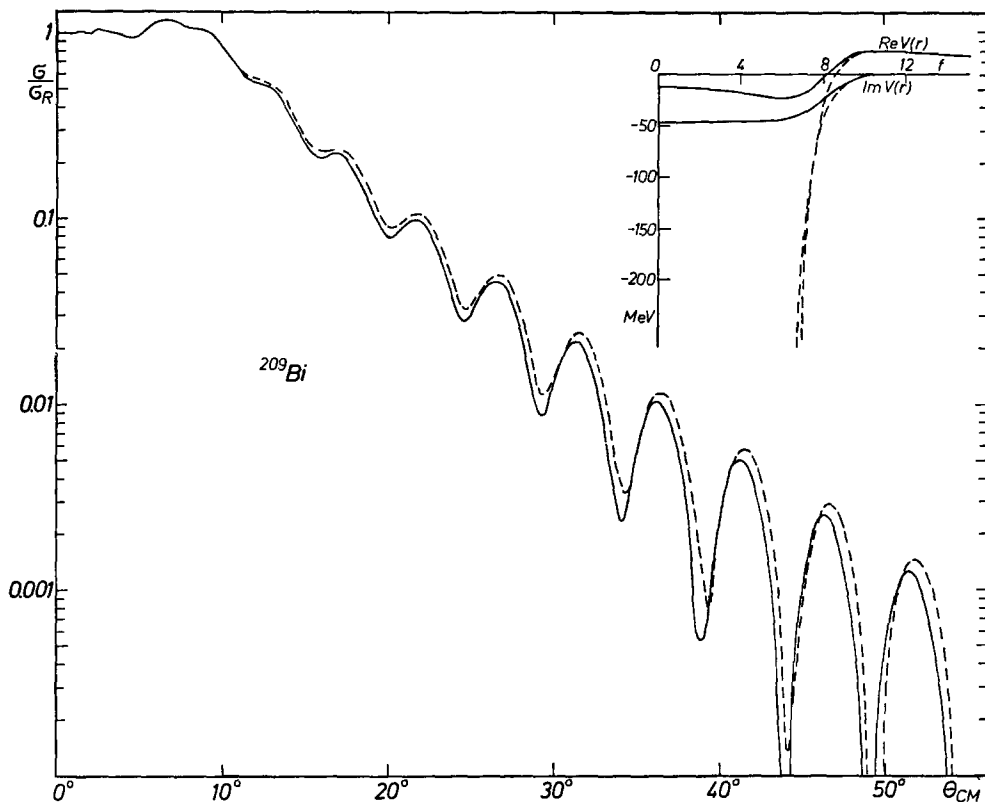


Fig. 15. Influence of the nuclear interior on the elastic scattering of 104 MeV alpha particles by ^{209}Bi .

4.3. MODEL INDEPENDENT IMPROVEMENTS OF THE FITS

The best fits obtained with the two models, phase-shift function and optical potential, are in good agreement with the experimental cross sections, but significant statistical deviations are still present. These deviations are a consequence of the simplifying assumptions made in the models applied. Now we drop these assumptions and try to correct each single partial scattering amplitude. The correction of the S_l values will reduce the systematic deviations between the experimental and calculated cross sections.

The minimum correction is obtained assuming that the argument $\alpha(\theta)$ of the experimental scattering amplitude

$$f_{\text{exp}}(\theta) = [\sigma_{\text{exp}}(\theta)]^{\frac{1}{2}} \exp [i\alpha(\theta)],$$

is the same argument as that of the scattering amplitude $f(\theta)$ of the best fit. Expanding $f_{\text{exp}}(\theta)$ according to expression (1), but with the coefficients $S_{l,\text{exp}}$, the cor-

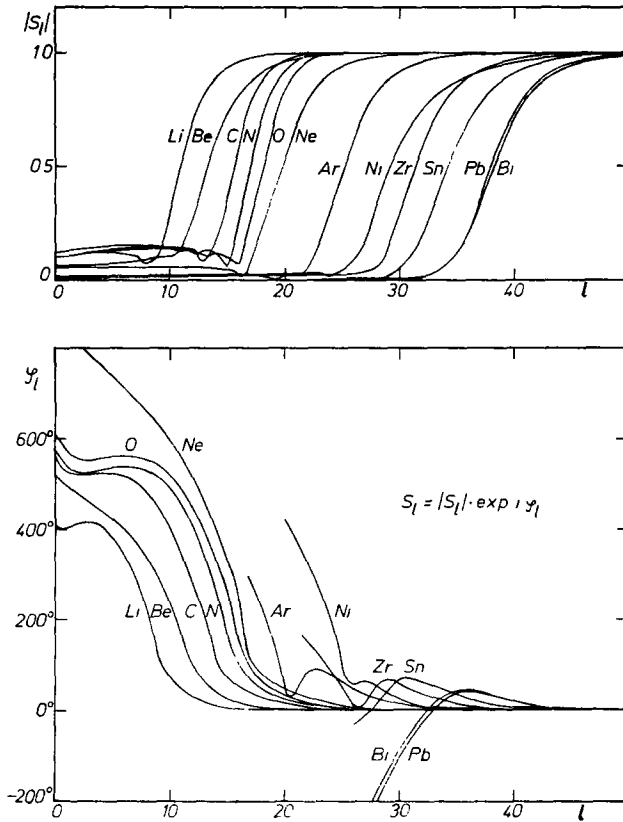


Fig. 16. Phase-shift functions obtained from the optical-model fits.

rections $\Delta S_l = S_{l,\text{exp}} - S_l$ can be obtained from the difference of the scattering amplitudes

$$\Delta f(\theta) = f_{\text{exp}}(\theta) - f(\theta),$$

$$\Delta f(\theta) = (2ik)^{-1} \sum_{l=0}^{\infty} (2l+1) \Delta S_l \exp(2i\sigma_l) P_l(\cos \theta). \quad (14)$$

Hence

$$\Delta S_l = ik \exp(-2i\sigma_l) \int_0^\pi \Delta f(\theta) \sin \theta P_l(\cos \theta) d\theta. \quad (15)$$

TABLE 4
Parameters for the best fits with the optical-model calculations

Target	R_v (fm)	a_v^- (fm)	a_v^+ (fm)	$-V_0$ (MeV)	R_w (fm)	a_w^+ (fm)	$-W_0$ (MeV)	χ^2/F	Model ^{a)}	σ_R (b)
^6Li	1.443	1.312	2.760	72.40	2.658	2.278	17.03	2.40	7	0.749
^9Be	2.103	∞	2.558	59.20	1.950	2.940	22.59	2.92	7	0.855
^{12}C	3.281		0.6921	74.21			30.23	18.34	4	0.832
^{12}C	2.139	∞	2.779	74.04	3.728	1.637	13.81	13.97	6	0.844
^{12}C	2.074	2.159	2.836	74.92	3.843	1.599	12.38	7.37	7	0.844
^{14}N	2.470	2.275	2.740	73.67	4.201	1.409	12.27	21.67	7	0.911
^{16}O	2.537	2.362	2.808	73.95	4.364	1.417	12.19	28.05	7	0.964
^{20}Ne	2.362	∞	2.944	84.45	3.941	2.156	16.95	3.12	6	1.129
^{40}Ar	3.130	∞	3.051	94.95	4.718	2.179	20.24	19.85	6	1.487
^{64}Ni	4.911	∞	2.538	39.98	5.451	2.812	13.06	16.74	6	1.929
^{64}Ni	4.694	∞	2.216	88.55	4.253	3.430	22.00	16.09	6	1.979
^{90}Zr	5.448	∞	2.533	47.43	5.838	2.542	18.37	3.62	6	2.032
^{124}Sn	6.896		0.7423	60.00			40.88	8.44	3	2.375
^{208}Pb	8.246		0.6556	60.00			43.85	8.90	3	2.746
^{209}Bi	8.118		0.7017	63.98			46.34	2.26	4	2.788

^{a)} The number indicates the number of free parameters.

Model 3, 4: The meaning of the parameters is given by expression (11) with $R = R_v$ and $a = a_v$.

Model 6, 7: The meaning of the parameters is given by expression (12).

F = number of degrees of freedom.

The integrand of integral (15) becomes zero for small scattering angles. Hence, the lower integration limit can be set equal to the smallest scattering angle measured. For large scattering angles the cross section drops rapidly to very small values. Therefore, the contribution of the large scattering angles is assumed to be negligible. Hence, the integration interval was chosen to be equal to the experimental angular range. In practical calculations the difference function $\Delta f(\theta)$ was interpolated linearly between the experimental points.

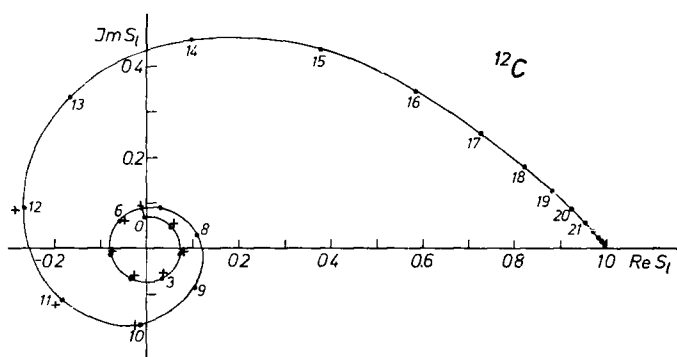


Fig. 17. Phase-shift function (solid curve) obtained from the phase-shift analysis of the ^{12}C data. The crosses show the corrected S_l values.

As an example fig. 17 shows the resulting corrections of the partial amplitudes for ^{12}C . The solid curve connects the S_l values of the best fit from the phase-shift analysis, the crosses represent the corrected amplitudes. Only the corrections for angular momentum numbers less than 13 are appreciable. The corrected S_l values scatter around the S_l function of the best fit. This behavior cannot be reproduced by the models used. The improvements achieved are demonstrated in fig. 18 for the light nuclei; the corrected χ^2 values are listed in table 3.

Furthermore, the corrections offer an estimate of the accuracy of the S_l values. Any successful model should reproduce the experimental cross section to an accuracy equal to the experimental errors. In this case the relative experimental errors are an upper limit of the errors of the S_l values. If a fit within the experimental errors cannot be achieved the relative deviations between the experimental cross section and the fit are an upper limit of the errors of the S_l values.

In addition, eq. (15) can be modified in order to indicate ambiguities in the phase-shift analysis. The argument of the scattering amplitude cannot be determined from the elastic scattering alone. Therefore, we can define a difference function

$$\Delta f(\theta) = f_2(\theta) - f(\theta),$$

such that

$$|f_2(\theta)| = |f(\theta)|,$$

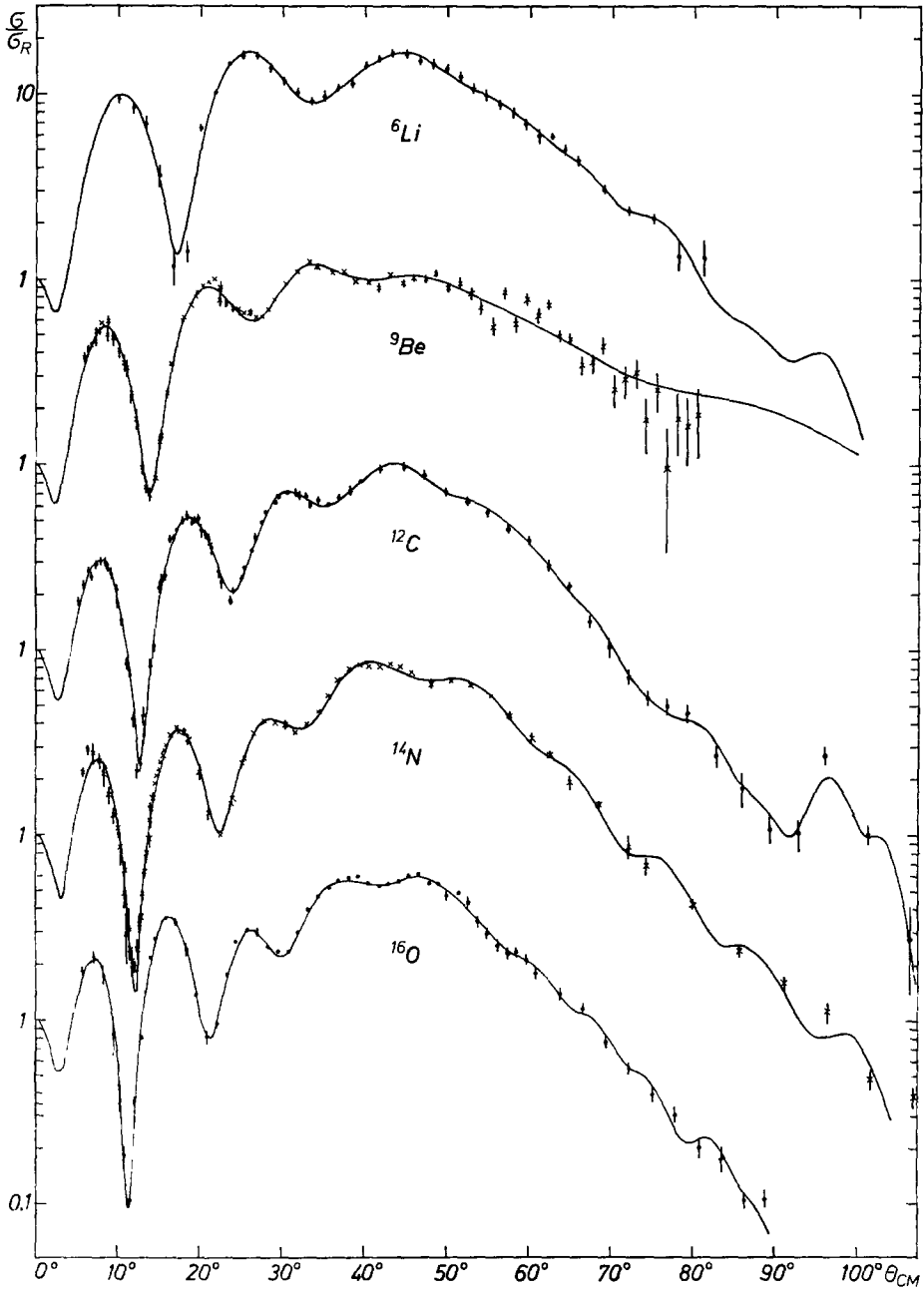


Fig. 18. Cross sections calculated from the corrected phase-shift analysis for the light nuclei.

in the experimental angular range and

$$\arg \Delta f(\theta) \rightarrow 0 \quad \text{for } \theta \rightarrow 0,$$

in order to preserve the normalization to the Rutherford scattering.

In this way other S_l functions may be obtained by inserting $\Delta f(\theta)$ in the integral (15) which leads to the same cross section. On the new S_l function some restrictions due to its physical interpretation must be done:

$$\begin{aligned} |S_l| &\leq 1 && \text{for all } l, \\ S_l &\rightarrow 1 && \text{for large } l. \end{aligned}$$

The phase shift and optical model fits of the ${}^6\text{Li}$ and ${}^9\text{Be}$ cross sections are equally good but the resulting phase-shift functions differ significantly (compare figs. 7 and 16). The phase-shift functions satisfy the restrictions due to their physical interpretations. Hence, we have an ambiguity due to the unknown $\arg f(\theta)$.

5. Discussion

The results of the phase-shift analysis show that the measured scattering cross sections may be described by an almost smooth phase-shift function as given by eq. (10) in section 4.1. The phase shifts are complex for low angular momentum numbers l as expected from the large number of open reaction channels, the partial amplitudes S_l are restricted to the physically meaningful region: $|S_l| \leq 1$. The correction procedure presented in subsect. 4.3 manifests some more detailed features. The S_l values deduced in the frame of the models must be corrected slightly in order to improve the agreement between experimental and theoretical cross-section curves. The corrections are small but indicate that the used parametrization is still too simple and has not enough degrees of freedom. The corrections to the partial scattering amplitudes are proportional to the relative deviations between the experimental and the theoretical scattering cross sections. Hence, an estimate of the accuracy of the S_l values is given.

Furthermore, the correction procedure elucidates the question of uniqueness of the resulting S_l values. Several different S_l sets may describe the same cross section as discussed in subsect. 4.3.

From optical-model analyses it is concluded that the elastic scattering of 104 MeV alpha particles on light nuclei may be described by a local potential containing a repulsive inner core added to the larger attractive well. Such a repulsive core which is explained by the nonlocal character of the true alpha-nucleus interaction³⁵) was previously only seen in the scattering of alpha particles on helium¹⁵). As shown in fig. 13 precise measurements are necessary to detect the repulsive core.

For the heavier nuclei the lack of transparency and the resulting ambiguities prevent an insight into the central region of the interaction potential. The ambiguities

of the optical-model analysis are twofold: a) the well-known phase ambiguity for the wave function in the medium weight nuclei. The two parameter sets given for the ^{64}Ni potential in table 4 demonstrate this case; b) the continuous ambiguity in the potential depths for the heavy nuclei as a consequence of the strong absorption; the nuclear interior remains invisible.

These facts influence the question of nuclear radii. The pronounced diffraction pattern of the angular distributions allows to extract radii in the l -space. In table 3 the cut-off angular momentum number L is given. In the optical model approach an answer is more difficult. Comparing the real and imaginary part of the interaction potential one clearly sees in fig. 12 that the radius (at half maximum) of the real part is smaller than that of the imaginary part. Nevertheless both nuclear potential parts have the same range and it is evident that a criterion is needed to compare the two radii. The radius may be defined as a half maximum radius or by use of the energy scale e.g. as a 5 MeV radius. In the case of strong absorption for the heavy nuclei, where the potential maximum remains unknown, a half maximum radius cannot be stated.

A common feature of our results obtained from the analysis is the following: The presented theoretical curves resulting from the best fits describe the cross sections in the experimental range, but they may differ at larger angles. As an example compare the ^{64}Ni curves in figs. 4 and 10. Due to the increased sensitivity to the scattering mechanism large angle scattering will provide a tool to the study of models in more detail.

We are indebted to Prof. Dr. O. Haxel for his interest in this work and wish to acknowledge stimulating discussions with the team of Prof. Dr. U. Schmidt-Rohr (MPI Heidelberg). We thank cand. phys. D. Habs for his help during the measurements, Mrs. G. Hoffmann for her help in data handling and the cyclotron staff for their good cooperation. The Bundesministerium für Wissenschaftliche Forschung has supported this research with equipment.

References

- 1) J. Alster, D. C. Shreve and R. J. Peterson, *Phys. Rev.* **144** (1966) 999
- 2) H. W. Broek, T. H. Braid, J. L. Yntema and B. Zeidman, *Nucl. Phys.* **38** (1962) 305
- 3) H. W. Broek, T. H. Braid, J. L. Yntema and B. Zeidman, *Phys. Rev.* **126** (1962) 1514
- 4) H. W. Broek and J. L. Yntema, *Nucl. Phys.* **64** (1965) 259
- 5) G. Bruge, CEA-R Report No. 3147 (1967)
- 6) G. Bruge, J. C. Faivre, H. Faraggi, G. Vallois, A. Bussi re and P. Roussel, *Phys. Lett.* **20** (1966) 293
- 7) R. F. Leonard, W. M. Stewart and N. Baron, *Phys. Rev.* **162** (1967) 1125
- 8) R. J. Peterson, *Phys. Rev.* **140** (1965) B1479
- 9) RLO Report No. 1388 **13** (1966) p. 10
- 10) RLO Report No. 1388 **23** (1967) p. 6 and 10
- 11) J. L. Yntema and G. R. Satchler, *Phys. Rev.* **161** (1967) 1137
- 12) C. R. Bingham, M. L. Halbert and R. H. Bassel, *Phys. Rev.* **148** (1966) 1174

- 13) P. Darriulat, G. Igo, H. P. Pugh, J. R. Meriwether and S. Yamabe, *Phys. Rev.* **134** (1964) B42
- 14) B. G. Harvey, E. J.-M. Rivet, A. Springer, J. R. Meriwether, W. B. Jones, J. H. Elliott and P. Darriulat, *Nucl. Phys.* **52** (1964) 465
- 15) P. Darriulat, G. Igo, H. G. Pugh and H. D. Holmgren, *Phys. Rev.* **137** (1965) B315
- 16) D. J. Horen, J. R. Meriwether, B. G. Harvey, A. Bussière de Nercy and J. Mahoney, *Nucl. Phys.* **72** (1965) 97
- 17) G. Hauser, R. Löhken, H. Rebel, G. Schatz, G. W. Schweimer and J. Specht, *Phys. Lett.* **27B** (1968) 220
- 18) R. M. Eisberg and C. E. Porter, *Rev. Mod. Phys.* **33** (1961) 190
- 19) G. Igo, *Phys. Rev.* **115** (1959) 1665
- 20) R. M. Drisko, G. R. Satchler and R. H. Bassel, *Phys. Lett.* **5** (1963) 347
- 21) W. J. Thompson, G. E. Crawford and R. H. Davis, *Nucl. Phys.* **A98** (1967) 228
- 22) A. Akhiezer and I. Pomeranchuk, *J. Phys. (USSR)* **9** (1945) 471
- 23) J. S. Blair, *Phys. Rev.* **95** (1954) 1218
- 24) W. E. Frahn and R. H. Venter, *Ann. of Phys.* **24** (1963) 243
- 25) E. V. Inopin, *Sov. Phys. JETP* **21** (1965) 1090; *ZhETF (USSR)* **48** (1965) 1620
- 26) T. E. O. Ericson, *Preludes in theoretical physics*, ed. by A. de-Shalit, H. Feshbach and L. van Hove (North-Holland Publ. Co., Amsterdam, 1965) p. 321
- 27) D. Hartwig, W. Linder, M. E. Lösel, G. Schatz and H. Schweickert, *KFK-Report* 754 (1968)
- 28) E. A. Silverstein, *Nucl. Instr.* **4** (1959) 52
- 29) G. Hauser, R. Löhken, H. Rebel, G. Schatz, G. W. Schweimer and J. Specht, *KFK-Report* 871 (1968)
- 30) B. Buck, R. N. Maddison and P. E. Hodgson, *Phil. Mag.* **5** (1960) 1181
- 31) M. J. D. Powell, *Computer J.* **7** (1964) 303
- 32) G. W. Schweimer, unpublished report (1968)
- 33) H. E. Auerbach, *BNL Report No. 6562* (1962)
- 34) R. Herman and R. Hofstadter, *High-energy electron scattering tables* (Stanford University Press) 1960
- 35) M. W. Kermode, *Nucl. Phys.* **68** (1965) 93